ORIGINAL PAPER

Identifying spatial transitions in heterogenous granular flow

Liuchi Li[1] · José E. Andrade[1]

Abstract

It is well known that heterogeneous granular flows exhibit collisional, dense and creep regimes that can coexist in space. How to correctly predict and control such complex phenomena has many applications in both mitigation of natural hazards and optimization of industrial processes. However, it still remains a challenge to establish a predictive granular rheology model due to the lack of understanding of the internal structure variation across different regimes and its interaction with the boundary. In this work, we use DEM simulations to investigate the internal structure of heterogeneous granular flow developed at the center of rotating drum systems. By systematically varying the side wall conditions, we are able to generate various heterogeneous flow fields under different levels of boundary effects. Our extensive simulation results reveal a highly relevant micro-structural quantity $\delta\theta = |\theta_c - \theta_f|$, where θ_c and θ_f are the preferred direction of inter-particle contacts and the preferred direction of inter-particle force transmissions, respectively. We show that $\delta\theta$ can characterize the internal structure of granular flow in collisional, dense and creep regimes, and its variation can identify the transition between them. In particular, in dense and collisional regimes, the classical rheological relation between bulk friction μ and inertia number I holds, while in the creep regime, such relation breaks down and μ instead depends on $\delta\theta$. Our findings hold for all investigated flow fields regardless of the level of boundary effect imposed, and regardless of the amount of shear experienced. $\delta\theta$ thus provides a unified micro-structural characterization for heterogeneous granular flow in different regimes, and lays the foundation of establishing microstructure-informed granular rheology models.

Keywords Heterogeneous flows · Spatial transitions · Experiments · Simulations · Microstructure

1 Introduction

Granular materials, collections of solid frictional grains with size greater than one micrometer, are ubiquitous on earth. The existence of static friction, negligible thermal effect and inelastic particle collision lead to their distinct ability of behaving like solids, liquids or gases [1]. In particular, when behaving like liquids, it has been observed that, both experimentally and numerically in various geometries [2–6], they often depart from homogeneous flow and exhibit co-existing regimes [7] that range from collisional to dense to creep flow. How to model and further control such feature of co-existing regimes has been of major research interest over the past decades because it would benefit not only the mitigation

of natural hazards such as snow avalanches, but the optimization of industrial processes such as silo discharge.

Based on the seminal $\mu(I)$ constitutive relation [8–10], and the observations of granular cluster formation [5, 11–14], several models have been proposed that could capture experimental observations by incorporating the concept of spatial correlation (giving rise to the so-called "non-local" rheology models) [15–17]. Here $\mu = \tau/P$ is the bulk friction with τ the shear stress and P the pressure; $I = \dot{\gamma}\bar{d}\sqrt{\rho_s/P}$ is called the inertial number with $\dot{\gamma}$ the shear rate, $\bar{d}$ the (mean) particle diameter and ρ_s the material density (see [9, 10] for details). Despite these theoretical advances, however, non-local effects are furnished into the $\mu(I)$ rheology by invoking phenomenological arguments that are still under debate [18–20]. The challenge lies in resolving the following three issues. First, in order to be valid, these models require stationary flow to further become steady (large amount of shear deformation), excluding their applicability to geometries containing flowing layers that are only stationary [21], such as creep flow in a rotation drum [22], in a silo [6] or over

✉ José E. Andrade
  jandrade@caltech.edu

[1] Division of Engineering and Applied Science, California Institute of Technology, Pasadena, CA 91125, USA

a heap [3, 23]. Second, the effects of boundary conditions on non-local phenomena are poorly understood—non-local phenomena can happen either with or without the presence of boundaries. For example, in "Kolmogorov flow" non-local phenomena manifest with periodic boundary conditions [20], while in planar shear flow [24] without stress gradient, non-local phenomena [25] can be triggered by the presence of rigid side walls. Lastly, it still remains unclear when and where non-local phenomena become significant. Resolving these three issues requires a fundamental understanding of (1) the internal structure variation of granular flow in collisional, dense and creep regimes, and (2) the dependence of internal structure variation on the amount of shear experienced and on boundary conditions. Only with such an understanding can we move forward to investigate the physical mechanism of non-locality, and eventually establish granular rheology models with a unified underlying mechanism.

To achieve such an understanding on the internal structure variation and its dependence on the amount of shear experienced and on boundary conditions, one will need to carefully choose a geometry that satisfies the following three requirements: (1) it should develop flow residing in all three regimes allowing non-local phenomena to arise at certain locations, (2) in the creep regime it should produce flow to be either just stationary or further steady, and (3) it should allow flexible control over boundary effects [26, 27]. In light of this we choose to investigate 3D flow developed at the center of rotating drums with large enough radius ($D/\bar{d} > 100$ [28]): we can produce spatially heterogeneous flow with stationary and steady creep flow layers coexisting in space, and further we can adjust the levels of imposed boundary effects by systematically varying the drum configurations (drum width and side wall friction). In particular, heterogeneous flow free of boundary effect is achievable numerically by using periodic side walls. In this work we for now focus our attention on nearly mono-disperse, (quasi) spherical and rigid particles: we first perform experimental measurements on the dynamics of glass beads flowing in a rotating drum, we then use these measurements to calibrate and validate our DEM model, and we lastly use this DEM model to probe various flow fields, by both changing the rotating speeds and the drum configurations. Despite having only studied one geometry, the obtained flow fields are general enough to be comparable to those produced under other geometries.

We propose a micro-structural quantity called $\delta\theta = |\theta_c - \theta_f|$, which we can define as the overall misalignment between the preferred direction of contacts (θ_c) and the main direction of inter-particle force transmissions (θ_f). We show that (1) $\delta\theta$ naturally identifies the spatial transition between collisional, dense and creep regimes, and (2) μ depends on $\delta\theta$ instead of I in the creep regime where the

one-to-one $\mu(I)$ relation breaks down. These findings hold regardless of the studied rotating speeds and drum configurations (with or without boundary effects), and hold in the creep regime regardless of the amount of shear experienced. Accordingly, our findings are not only applicable to similar geometries (such as heap flows [3, 23]) where shear deformation can be largely absent, but relevant to other geometries (such as planar flows with gravity [29]) where steady creep flow occurs and is believed to be triggered by steady state non-local effects. Our results suggest that, the misalignment between θ_c and θ_f in the creep regime can be caused by either (1) steady-state non-local effects or (2) lack of shear deformation. Further investigations to distinguish or to find connections between the two will be helpful in establishing micro-structure-informed granular rheology models.

2 Experiments

We half-fill a drum with quasi-spherical soda lime glass beads with density $\rho_s = 2450 \, \text{kg/m}^3$, roundness $\geq 95\%$, and particle diameter $d = 1-1.25 \, \text{mm}$. The drum has inner diameter $D = 277 \, \text{mm} \simeq 246\bar{d}$ and inner width $W_0 = 25 \, \text{mm} \simeq 22\bar{d}$, where $\bar{d} = 1.125 \, \text{mm}$. The front-side of the drum is bounded by a transparent circular glass plate allowing for optical measurement, while the rear-side and inner-cylinder walls have glass beads glued to them (accordingly the effective drum width is $W \simeq 21\bar{d}$). Different rotation speeds ω can be imposed in the experiments, ranging from 0.21 to $11.23°/\text{s}$. In this work we consider three different rotation speeds: $\omega = 2.59°/\text{s}, 5.73°/\text{s}$ and $11.23°/\text{s}$. For each considered rotation speed, after 20 rotations, we take images via a high-speed camera (Phantom V310, fps = 1000 with image size 288 px × 288 px) throughout a time window of 10 s, and measure the dynamical angle of repose and down-stream velocity near the glass plate at the center of the drum. For information on how these measurements are performed, see "Appendix 1". The measured dynamical angle of repose and down-stream velocity are used to calibrate and validate our numerical model.

3 Discrete-element-method (DEM) simulations

We use DEM [30] implemented in the open-source code LIGGGHTS [31] to perform simulations, approximating glass beads by spheres that interact through Hookean contact law with Coulomb friction. Initially we consider a drum to share the same dimension as the one used in the experiments—the cylindrical wall and rear-side wall are made of spheres, and the front-side wall is treated as a flat plane, see Fig. 1. Assuming the diameter following a Gaussian

Fig. 1 From left to right: simulation setup in accordance with the drum used in the experiments (front plane not shown); region at the drum center for data extraction; (weakly) poly-disperse spheres with their computed radical Voronoi diagram that is used to compute the volume fraction ϕ
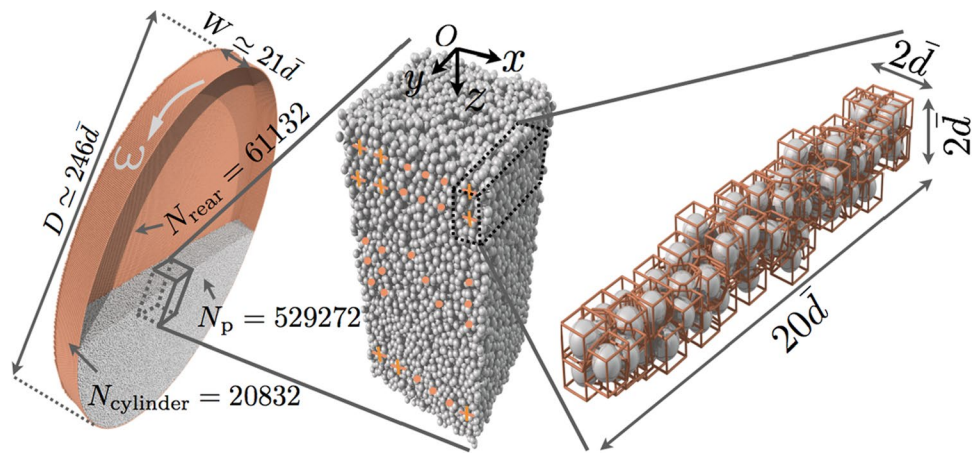
distribution $d \sim \mathcal{N}(1.125, 0.04^2)$, we sample spheres used as walls ($N_{\mathrm{rear}} = 61132, N_{\mathrm{cylinder}} = 20832$), and as granular medium ($N_{\mathrm{p}} = 529272$). We have also tried a uniform distribution from 1 to 1.25 mm, and we found the results are insensitive to the chosen distribution regarding the particle diameter range considered in our study. The diameter range $d = 1-1.25$ mm is ensured by rejecting over and under-sized spheres. We calibrate and validate our model for flows developed at the drum center based on the aforementioned drum experiments (see "Appendix 1" for details). The determined value for each model parameter is: the normal stiffness $k_{\mathrm{n}} = 2 \times 10^5 \bar{m}g/\bar{d}$ with $\bar{m}$ the mean particle mass and g the gravitational constant, the tangential stiffness $k_{\mathrm{t}} = 2/7 k_{\mathrm{n}}$, the coefficient of restitution $e = 0.82$ [accordingly the normal damping $\gamma_{\mathrm{n}} = -2\ln e \sqrt{\bar{m}k_{\mathrm{n}}/(\pi^2 + \ln^2 e)}$], the tangential damping $\gamma_{\mathrm{t}} = 0$, and the surface friction coefficient $\mu_{\mathrm{p}} = 0.4$ with a rolling friction $\mu_{\mathrm{r}} = 0.03$. The friction coefficient between spheres and the front-side wall is also 0.4, with no rolling friction. The integration time step $\Delta t = t_c/10$ [32], where t_c is the binary collision time. Since the determined combination of values for these model parameters may not be unique depending on the specific calibration-validation procedure [33, 34], we do not rule out the possible existence of other combinations.

Based on the validated model, we perform two additional simulations with $\omega = 33.69°/$s and $67.38°/$s. Taking advantage of this novel asymmetrical side wall setup (one bumpy one flat) [10, 35–37], in order to include more flow conditions, we further consider different drum configurations, by either varying its width, or varying simultaneously the surface friction coefficient associated with the wall spheres and the front plane (hereafter we term both as the wall friction), with no change to the rolling friction. Specifically, we consider six different types of drum configurations: in four of them the wall friction is varied (first row in Table 1), while in the remaining two the effective drum width is varied (second and third row in Table 1). For each drum

Table 1 Considered drum configurations in our simulations

W_0 (mm)	$W/\bar{d}$	Wall friction
25	21	0.2, 0.4, 0.6, 0.8
24	∞	– (periodic)
12	10	0.4

For the periodic case, the cylindrical wall friction remains 0.4. Every configuration operates under five different rotation speeds $\omega = 2.59°/$s$, 5.73°/$s$, 11.23°/$s$, 33.69°/$s and $67.38°/$s

configuration we consider five different rotation speeds: $\omega = 2.59°/$s$, 5.73°/$s$, 11.23°/$s$, 33.69°/$s$, and $67.38°/$s. Accordingly we consider in total 30 different flow fields which have Froude number on the order of $10^{-5}-10^{-2}$. For these additionally performed simulations, even though we have not directly validated them against experiments, the simulated macro-scale flow responses are consistent with relevant studies. For instance, stronger side wall effect can lead to higher dynamical angle of repose [38, 39]. We use these simulation results to investigate both the macro-scale rheological responses and the micro-scale internal structure variations under different flow conditions.

For each simulation, after the flow becomes stationary, we output data for analysis. We choose the reference frame to be located at the drum center and to rotate with the drum, with the y (z) axis being parallel (perpendicular) to the local free surface (Fig. 1). Note that while the local free surface remains flat, the whole surface profile can show an "S-shape" [39], see "Appendix 2". We consider flow at the drum center where the local surface remains flat for easy data extraction, and where the cylindrical wall effect is negligible [28] (we have $D/\bar{d} > 100$). In particular, as briefly mentioned in the introduction section, flow produced at the drum center can be essentially free of boundary effects once we set the side walls to be periodic. We first create a set of grid points (red crosses in Fig. 1) at the drum center ($y = 0$) that are equally-spaced by $\bar{d}$ in both the x and z directions: along the x

direction, they span from $x = -8\bar{d}$ to $x = 9\bar{d}$ ($W/\bar{d} \simeq 21$) and from $x = -3\bar{d}$ to $x = 4\bar{d}$ ($W/\bar{d} \simeq 10$); along the z direction they cover a depth down to $100\bar{d}$. We then consider a box ($L_y = 20\bar{d}, L_x = L_z = 2\bar{d}$) centered at $y = 0$, aligned with the y direction, surrounding each grid point to extract data. Some relevant fields are (1) the velocity v_i, (2) the shear rate $\dot{\gamma}_{ij} = (v_{i,j} + v_{j,i})/2$ (neglecting $\partial_y v_i$), together with the deviatoric part $\dot{\gamma}_{ij}^d = \dot{\gamma}_{ij} - \dot{\gamma}_{kk}\delta_{ij}/3$ and $|\dot{\gamma}^d| = \sqrt{2\dot{\gamma}_{ij}^d\dot{\gamma}_{ij}^d}$, (3) the Cauchy stress $\sigma_{ij} = \sum_c f_i^c \ell_j^c / V$ [40] together with $P = -\sigma_{kk}/3$, $s_{ij} = \sigma_{ij} + P\delta_{ij}$ and $\tau = \sqrt{s_{ij}s_{ij}/2}$, where V is the volume of every box and the summation is taken over all the contacts c with contact force f^c and branch vector ℓ^c connecting the centroids of contacting particles, and (4) the volume fraction ϕ by computing the radical Voronoi diagram using the open-source code Voro++ [41]. We confirm that (1) these quantities are insensitive to grid translation (either $y = -5d$ or $y = 5d$), box size ($L_x = L_z = \bar{d}$ or $3\bar{d}$) and grid spacing (50% or no overlap between boxes), (2) kinematical contribution to the stress tensor is negligible [9, 22, 25, 29] and (3) results computed using either $\dot{\gamma}$ or $\dot{\gamma}^d$ are essentially identical and we use $\dot{\gamma}^d$ throughout. Note that the values of all fields mentioned hereafter are the temporal average of instantaneous ones computed via spatial coarse-graining within each box. Lastly, hereafter in all figures, quantities are shown as drum-width-averaged values, with error bars representing the variation across drum width.

4 Simulation results and discussions

4.1 Rheological response

We first perform macroscopic observations following the $\mu(I)$ rheology [9, 10]: Fig. 2a, b show, respectively, the $\phi - I$ and $\mu - I$ relationships. The one-to-one relation between ϕ and I holds reasonably well, except for cases with $W/\bar{d} \simeq 10$, which can be attributed to stronger wall friction effects [42]. For all cases considered, the slow decrease of ϕ as I increases suggests the weak compressibility of steady dense

granular flows [10, 43]. In contrast, a one-to-one relation between μ and I holds globally, until I decreases to a certain I_{th} threshold. For locations with $I \leq I_{th}$, this one-to-one relation no longer holds globally but rather depends on both drum configuration and rotation speed. The threshold value of I_{th} varies on a case by case basis, but roughly resides in the range of 10^{-3}–10^{-2}, as shown in Fig. 2b. As we shall see later, as long as $I > I_{th}$, all $\mu - I$ data can actually be described by the $\mu - I$ frictional law [9, 10]. Additionally, we find that more frictional walls and narrower drums, tend to break the typically-observed co-directionality between s and $\dot{\gamma}^d$ (see "Appendix 2"). Hence, the rheological effect of side wall friction can be summarized as (1) when $I > I_{th}$, it leads to the break down of the co-directionality between s and $\dot{\gamma}^d$ (this could explain the deviation of predicted velocity from experimental measurements reported in [10]), and (2) when $I \leq I_{th}$, it not only intensifies the lack of co-directionality effect, but also signifies the departure from the one-to-one $\mu - I$ relationship. We have tried to explain the aforementioned observations using several existing non-local models [17, 29, 44], but unfortunately have not had much success (see "Appendix 2"). Clearly, these observations necessitate a deeper fundamental understanding of the spatial transition marked by I_{th}.

4.2 Microstructures and spatial transitions

Based on our observations of the rheological response, we perform particle-scale investigations to characterize the micro-structure of the flow. In principle, we are trying to find certain micro-structural quantities whose variations against I (1) exhibit a clear transition as crossing I_{th} and identify the location z_{th} corresponding to I_{th}, and (2) correlate with the macro-scale rheological response: when $I > I_{th}$ the spatial variations are free of drum configuration effects and rotation speed effects, while as soon as $I \leq I_{th}$ they become both drum-configuration-dependent and rotation-speed-dependent.

We propose a micro-structural quantity $\delta\theta = |\theta_c - \theta_f|$ (see Appendix section "Additional results from micro-scale

Fig. 2 **a** Effective friction μ and **b** volume fraction ϕ as a function of I
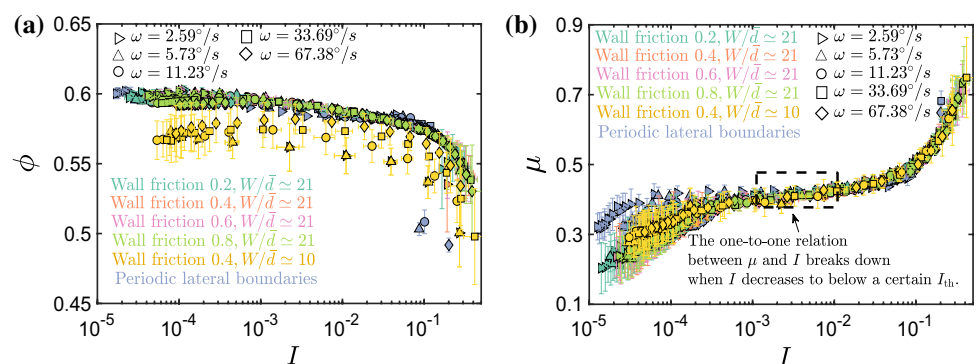
analysis" for additional results), where θ_c and θ_f are, respectively, the major principle direction of the "fabric" tensor (χ^c) and that of the "force-transmission" tensor (χ^f):

$$\chi_{ij}^c = \langle n_i^c n_j^c \rangle, \quad \chi_{ij}^f = \frac{1}{\langle |f| \rangle} \langle |f| n_i^c n_j^c \rangle, \tag{1}$$

where "$\langle \cdot \rangle$" denotes the average over all contacts, n^c is the contact normal which coincides with the branch vector direction for contact between spheres, $|f| = \sqrt{f_n^2 + f_t^2}$ is the associated contact force magnitude with f_n the normal component and f_t the tangential (frictional) component. Compared to χ^c, χ^f is a biased average in the sense that each contact is weighted by the magnitude of the force it carries. Mathematically $\delta\theta$ has range $[0, 90°]$. Physically, for dense particle packings, θ_c and θ_f reflect, respectively, the geometrical configuration of the packing and the direction of force chains. For every simulation, we find that the variation of $\delta\theta$ as a function of depth follows the same trend that can be described with four different layers—Fig. 3 showcases the variation of $\delta\theta$ against normalized depth with $\omega = 33.69°/\text{s}$ under respectively, $W/\bar{d} = \infty$ with periodic side wall condition (lower panel of Fig. 3a), and $W/\bar{d} \simeq 21$ with wall friction 0.4 (lower panel of Fig. 3b): the first layer, from near the free surface until a critical depth z_1, shows a decrease in $\delta\theta$. Next, a second layer that goes until a critical depth z_2 and where $\delta\theta$ remains *constant*. This is followed by

a third layer extending to a critical depth z_3, where $\delta\theta$ increases, and finally a fourth layer where $\delta\theta$ slowly relaxes. As we shall show later, this spatial variation of $\delta\theta$ can be used to identify different flow regimes. For depths $z > z_3$, where $\delta\theta$ ceases to increase but instead slowly relaxes along depth, we find the particle motions are highly intermittent and therefore can not be considered as stationary. We regard these regions as "static" and do not attempt to model them, considering particle motions on the basis of the random void creation process [3].

Although the values of z_1 and z_2 differ from case to case, we find that z_1 corresponds to the universal $I \simeq 0.1$ (Fig. 4a); z_2 coincides with z_{th} (Fig. 4b) and $\delta\theta \simeq 10°$ for $z_1 \le z \le z_2$ (Fig. 4a, b), where z_{th} is defined as the end point of the widely-observed exponential velocity profile [4, 22]. (See the upper panel of both Fig. 3a, b where the black solid lines indicate exponential fit, also see Appendix section "Determination of z_{th} based on the drum-width-averaged velocity profile" for why drum-width-averaged profiles suffice to determine z_{th}.)

We first consider the regime where $z \le z_2$. The identified universal value $I \simeq 0.1$ [25] at $z = z_1$ is critical since it signifies the transition from collisional flow ($z \le z_1$), where particles interact majorly through short-lived binary collisions, to dense flow ($z_1 < z \le z_2$), where particles interact mostly through percolating contact network. Specifically, we observe that in the dense flow region, $\delta\theta$ remains constant
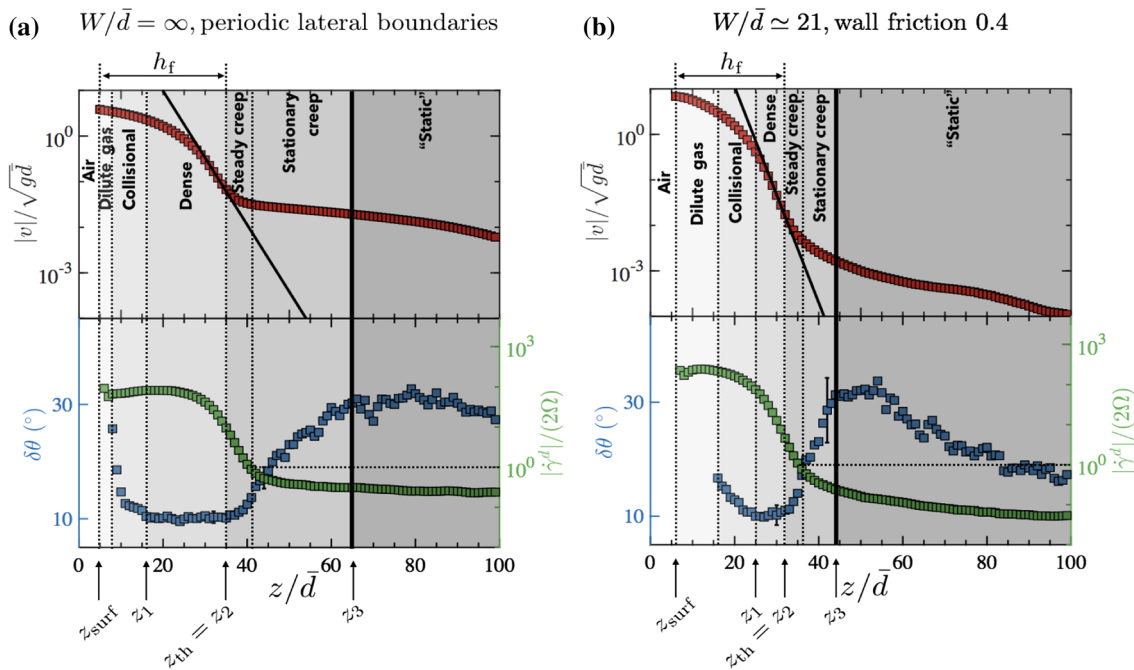

Fig. 3 **a** Under $W/\bar{d} = \infty$ with periodic side wall condition, the spatial variation of $|v|/\sqrt{g\bar{d}}$ (data in red at upper panel, with black solid lines indicating the exponential fit), of $\delta\theta$ (data in blue at lower panel, with error bars indicating its typical variation across drum width in both dense and creep regime), and of $|\dot{\gamma}^d|/2\Omega$ (data in green at lower panel) against normalized depth $z/\bar{d}$. **b** Same plots but under $W/\bar{d} \simeq 21$ with wall friction 0.4. We define a flow thickness (h_f) starting from the free surface (z_{surf}) to the end point of dense regime (z_2)
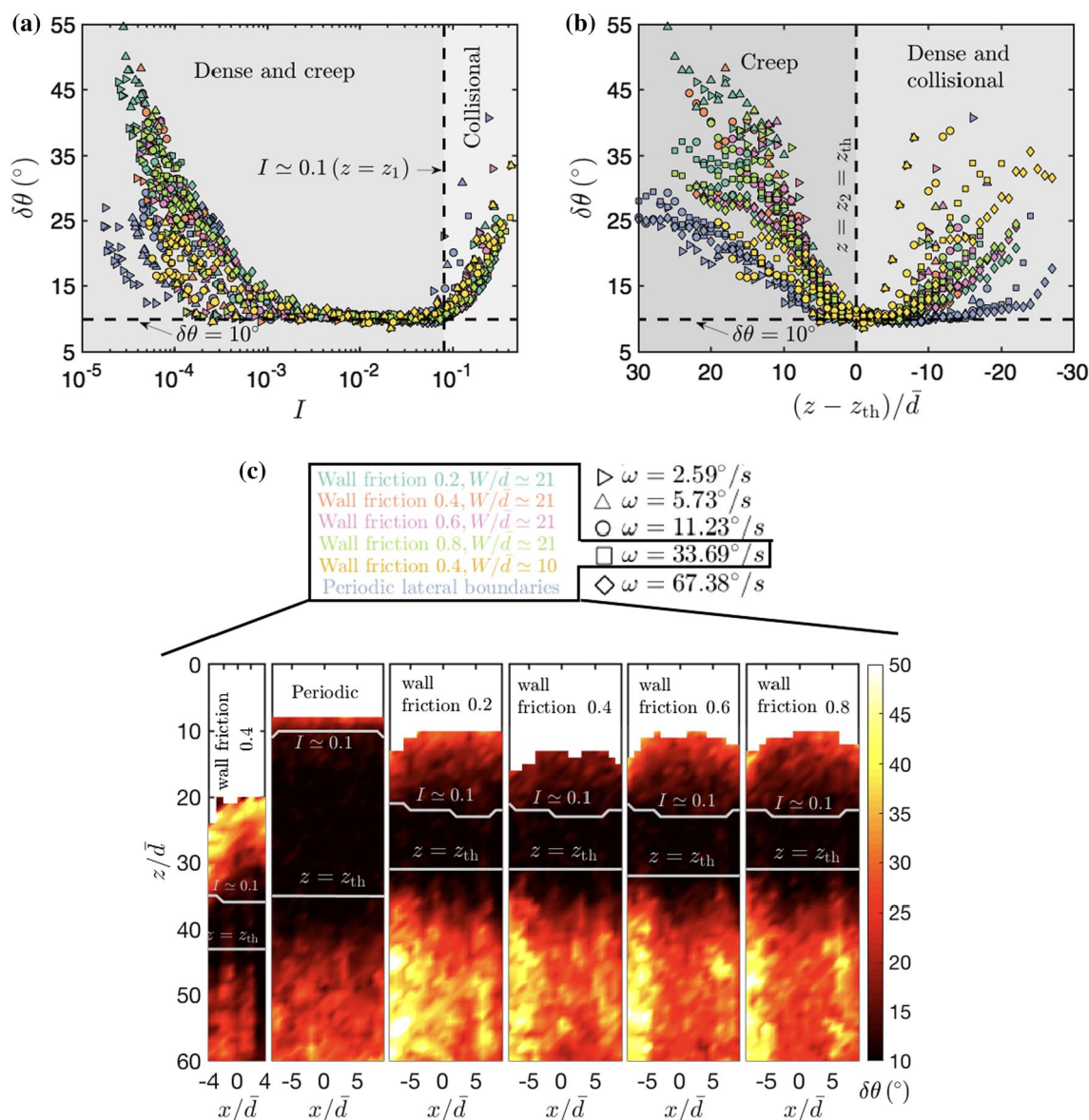
Fig. 4 **a** Variation of $\delta\theta$ against inertia number I for all cases from $z \leq z_3$. **b** Variation of $\delta\theta$ against depth z (normalized by z_{th} and $\bar{d}$) from $z \leq z_3$. **c** Spatial variation (along both x and z) of $\delta\theta$ for all cases under $\omega = 33.69°/\text{s}$; from left to right: frictional side walls ($W/\bar{d} \simeq 10$) with wall friction of 0.4, periodic side walls, and frictional side walls ($W/\bar{d} \simeq 21$) with wall friction of respectively 0.2, 0.4, 0.6 and 0.8

and small everywhere (Fig. 4c), even near the side walls regardless of how frictional they are, or whether they are bumpy or flat and how wide the drum is. In fact, the observed θ_c and θ_f being nearly co-directional has also previously been reported in numerical studies of dense homogeneous planar flows [25]. Lastly, in this regime the $\mu(I)$ rheology in its invariant form holds (Fig. 5a): we can fit the $\mu - I$ relation by both the linear [9, 45] and the non-linear formulation [10], although some deviation is observed for the latter for $I > 0.1$. On a side note, in all our simulations, within the collisional layer the highest inertia number value we are able to compute is around 0.3, beyond which, given the size of

our homogenization box and our sampling frequency, the temporal average can not be properly defined since particle interactions are largely absent in multiple snapshots. We thus define the additional layer on top of the collisional layer as belonging to the dilute gas regime (upper panel of Fig. 3a, b). We note that this value 0.3 has previously been identified as the point to transit into "fully collisional regime", where it has been shown that, the portion of floating particle (particle with no contact) in the system, goes beyond 0.6 [25]. In our study, we have consistent observation—looking at Fig. A6(a), the mean coordination number drops to nearly zero as approaching the dilute gas regime. Thus in the dilute gas

Fig. 5 a One-to-one relation between μ and I in collisional and dense regime, and that between μ and $\delta\theta$ in the creep regime. The $\mu - I$ data can be fit by both the linear law (black solid line) $\mu = \mu_s + bI$ with $\mu_s = 0.4148 \pm 0.0017$ and $b = 0.8628 \pm 0.0216$, and the non-linear law (black dashed line) $\mu = \mu_1 + (\mu_2 - \mu_1)/(1 + I_0/I)$ with $I_0 = 0.279$ (adapted from [10]), $\mu_1 = 0.4089 \pm 0.0023$ and $\mu_2 = 0.7643 \pm 0.0107$. Variation against rotation speed of **b** flowing thickness $h_{\rm f}$ and (c) $I_{\rm th}$ at $z = z_{\rm th}$
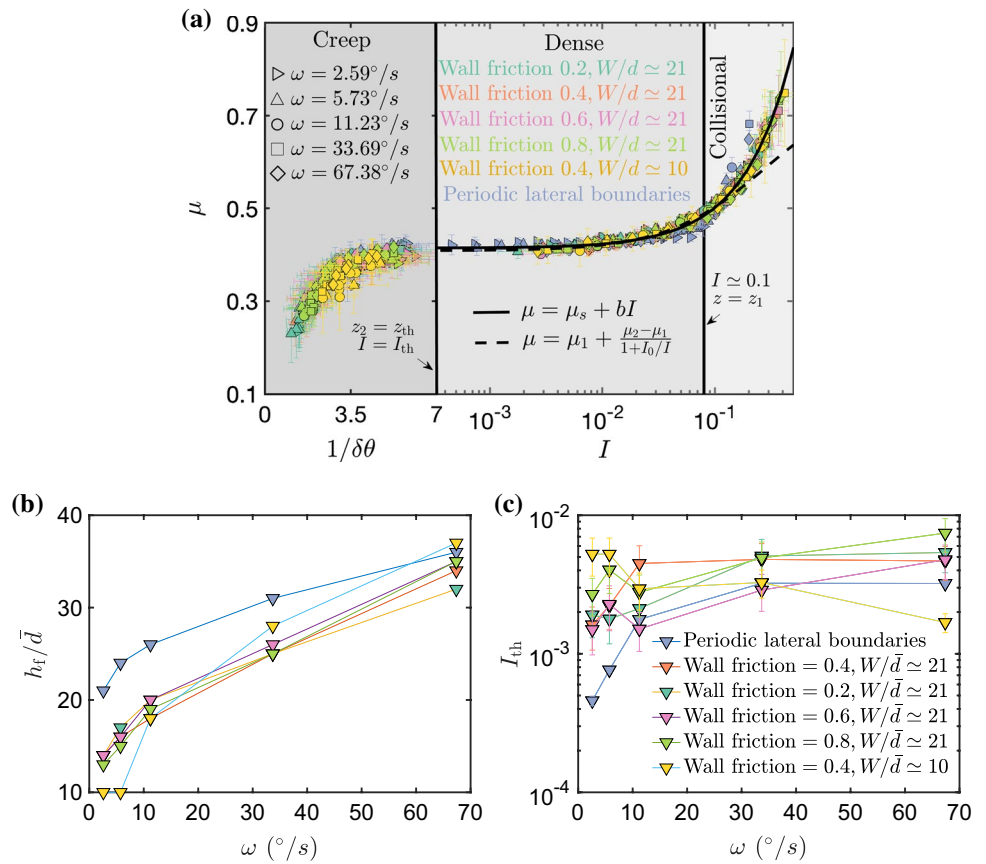
regime ("fully collisional regime"), the $\mu(I)$ rheological law no longer holds, and kinetic theory [46] becomes applicable.

We then consider the regime where $z_2 < z \leq z_3$. As soon as z goes beyond z_2, $\delta\theta$ starts increasing and the $\mu - I$ relationship breaks down—it turns out that $I_{\rm th}$ corresponds to the location $z = z_2 = z_{\rm th}$, where the misalignment between χ^c and χ^f begins, right at the end point of the exponential velocity profile. Thus, we identify this as the creep flow regime where μ has a one-to-one relation with $\delta\theta$ instead of I (Fig. 5a): μ is inversely proportional to $\delta\theta$. From a microstructural perspective, and for weakly poly-disperse sphere packings, μ can be well-approximated by adding together the contact anisotropy (determined from the eigenvalues of χ^c) and the force anisotropy (determined from the eigenvalues of χ^f) [25, 47]. Meanwhile, for a given packing configuration, with known contact anisotropy of direction θ_c, the force anisotropy is maximized if θ_f equals θ_c [48]: the larger the deviation of θ_f from θ_c, the smaller the force anisotropy and accordingly the smaller the μ. More importantly, we emphasize here that the dependence of μ on $\delta\theta$, and the increase of $\delta\theta$ in the creep regime hold regardless of the amount of shear experienced. In order to see this, we use the local deformation $|\dot{\gamma}^d|/2\Omega$ to determine whether the initial memory is gone (shear deformation is large enough). Similar to [21], as the drum is half filled

and the flow is stationary, we consider the shear deformation to be sufficient if $|\dot{\gamma}^d|/2\Omega > 1$, in other words, particles have entered the surface avalanche after half a drum rotation period and the initial packing memory is erased by the fast surface flow. We have observed that for all rotation speeds considered, in the creep regime, the presence of layers with local deformation being both greater than one (termed as steady creep flow layer) and less than one (termed as stationary creep flow layer). As an example, as showcased in Fig. 3a, b, under $\omega = 33.69°/s$ for two different drum configurations ($W/\bar{d} \simeq 21$ with wall friction 0.4 and $W/\bar{d} = \infty$ with periodic side walls), there is a layer (with thickness $3\bar{d}-5\bar{d}$) right after entering the creep regime where the local deformation is larger than one. In these layers, $\delta\theta$ is no longer constant, but rather increases with depth, and the one-to-one $\mu(I)$ relation breaks down. Similar steady creep flow layers with large shear deformation have also been observed in other geometries such as annular shear flow [43] and planar shear flow with gravity [29], in which the break-down of the one-to-one $\mu(I)$ relation is explained by steady-state non-local models. Following these steady creep flow layers deeper into the bulk are the stationary creep flow layers where the local deformation $|\dot{\gamma}^d|/2\Omega$ decreases to less than one. In these stationary creep flow layers the values of $\delta\theta$ continue to increase

with depth, and the values of μ keep depending on the values of $\delta\theta$. This result suggests that, the misalignment of force chain direction and preferred contact direction can be caused by either (1) steady-state non-local effect for steady creep flow or (2) lack of shear deformation for stationary creep flow. Further investigations need to be carried out to distinguish or find connections between the two. For example, it will be helpful to adopt a Lagrangian perspective, where we perform investigations by tracking the trajectory of each particle and examining its correlation with the inter-particle force network.

Figure 5b, c show the variation of flow thickness $h_f = z_2 - z_{surface}$ and I_{th} against ω. We observe that the effective drum width W has a stronger effect than side wall friction in changing h_f. However its influence seems to decrease as ω increases. The value of I_{th} can not be determined by a single constant as in [44], but depends on the specific drum configuration and rotation speed. In general, weaker boundary effect (larger effective drum width or smaller wall friction) and smaller rotating speed lead to smaller values of I_{th}, in other words, weaker boundary effect and smaller rotation speed can extend the applicability of the classical $\mu(I)$ rheological relation to flows with smaller values of I. This observation is supported by our results from cases with the effective drum width W being around $21\bar{d}$ under different wall friction, and being infinite under periodic side walls. One way to rationalize this is to consider steady state non-local effect, where particles in the creep flow layers may be "agitated" by particles in the fast flowing layers near the free surface. The faster the particles flow in dense and collisional regime, the larger the force fluctuations can they generate to "agitate" particles, presumably via force chains, in the underlying creep regime. As the presence of side wall friction and larger rotation speed can generate faster surface flow, the transition into creep regime (where the $\mu(I)$ relation breaks down) can happen with a larger value of I_{th}. However, for cases with $W/\bar{d} \simeq 10$ the dependence of I_{th} on drum configuration and rotation speed becomes a bit more complicated. At smaller rotation speeds ($\omega \leq 5.73°/s$) we have consistent observations—the values of I_{th} are at least non-decreasing with increasing rotation speeds, and are larger than those computed from wider drums due to stronger boundary effect. Whereas for larger rotation speeds ($\omega \geq 11.23°/s$), values of I_{th} start to decrease with increasing rotation speeds. Further, at the highest rotation speed ($\omega = 67.38°/s$) the value of I_{th} decreases to be even smaller than that computed from periodic side wall conditions. We attribute this observation to the influence of effective wall friction [36] which becomes more pronounced under larger rotation speeds, subsequently leading to a faster decay of I along depth than those computed from wider drums. As a consequence values of I can decrease for an order of magnitude when crossing I_{th}, giving values of I_{th} that decrease with increasing rotation speeds, and giving values of I_{th} that can become smaller than those computed from wider drums.

5 Concluding remarks

We propose a micro-structural quantity called $\delta\theta$ whose spatial variation characterizes the internal structure of granular flow in different regimes: (1) it recovers the universal value $I \simeq 0.1$ that corresponds to the transition ($z = z_1$) from collisional regime to dense regime [25] and, more importantly, (2) it identifies the boundary ($z = z_2 = z_{th}$) between dense regime and creep regime with the value of $\delta\theta$ governing the variation of μ in the creep regime. The universal value $I \simeq 0.1$ and the both drum-configuration-dependent and rotation-speed-dependent I_{th} are closely related to the respective underlying particle interaction mechanisms: spatially uncorrelated and short-lived binary collisions for I above 0.1 and spatially correlated and enduring contact networks for I below I_{th}.

These findings hold regardless of studied rotating speeds and drum configurations (with or without boundary effects), and hold in the creep regime regardless of the amount of experienced shear deformation. Our findings are thus not only applicable to similar geometries (such as heap flows [3] and silo flows [6]) where shear deformation can also be largely absent in the creep regime, but relevant to other geometries (such as planar flows with gravity [29]) where steady creep flow with large enough shear occurs and is believed to be triggered by steady state non-local effects. $\delta\theta$ thus provides a unified interpretation of the internal structure of granular flow in all three regimes. In particular, in the creep regime, it suggests that the misalignment between force chain direction and preferred contact direction can be caused by either (1) steady-state non-local effect, or (2) lack of shear deformation. Further investigations to distinguish or to find connections between them, will be helpful in establishing microstructure-informed granular rheology models with a unified underlying mechanism.

In the future, we plan to extend our work to more realistic (and more complicated) granular materials by gradually adding ingredients like shape [49–51], deformability [19, 23], and polydispersity [52, 53]—these new ingredients may lead to different interaction mechanism not only between particles, but between particles and boundaries [54].

Compliance with ethical standards

Appendix 1: Discrete element model calibration and validation

In this section we discuss how we determine the model parameters used in our simulations. In general, the interaction between rigid particles can be modeled by either solving a linear-complementarity problem (implicit dynamics, the NSCD) [55] or by penalizing the interparticle penetration (explicit dynamics, the classical DEM). Despite the different underlying principle, they give consistent results within the scope of rigid particle dynamics [56]. For the classical DEM, there are various inter-particle contact laws with different level of sophistication. Following the discussion in [57], we choose the linear Hookean contact law and pick $k_n = 2 \times 10^5 \bar{m}g/\bar{d}$ (large enough to ensure rigid particle limit for the gravity-driven surface flows considered in our study) with $k_t = 2/7k_n$, $\gamma_t = 0$, and $\gamma_n = -2\ln e\sqrt{\bar{m}k_n/(\pi^2 + \ln^2 e)}$. We are left to determine the coefficient of restitution e, the inter-particle friction μ_p, the particle-wall friction and possibly the addition of rolling friction μ_r.

First stage calibration via column collapse tests

We use the column collapse test to perform preliminary model calibration by measuring the angle of repose θ_r. We first glue glass beads to the center area of an aluminum sheet (300×300 mm) and the inner surface of two identical iron angle bars with height 50 mm, length 25 mm and width 16 mm (Fig. 6a). A typical column collapse test can be divided into three steps: (1) filling with glass beads the hollow rectangular tube formed by the two iron angle bars placed over the aluminum sheet center, (2) rapidly removing the bars, and (3) taking picture of the formed pile to measure θ_r. We repeat the procedure for 50 times and θ_r is measured to have a mean of 13.87° and a standard deviation of 0.576°.

Via DEM simulations, we then perform numerical column collapse tests with the same configuration as in the experiments. We carry out two sets of simulations: (1) fixing $\mu_p = 0.4$ (a common choice for glass beads) and varying e from 0.1 to 0.82, and (2) fixing $e = 0.82$ [58] and varying μ_p from 0.1 to 0.8. From (1) we find that e has negligible effect on θ_r (Fig. 6c), and from (2) that θ_r first increases but later saturates with the increase of μ_p (Fig. 6b). In summary the above results suggest the necessity to incorporate rolling friction μ_r, a parameter that imposes rotation hinderance [59] to model the interaction between non-spherical particles. Accordingly, we fix $e = 0.82$, $\mu_p = 0.4$ and vary μ_r from
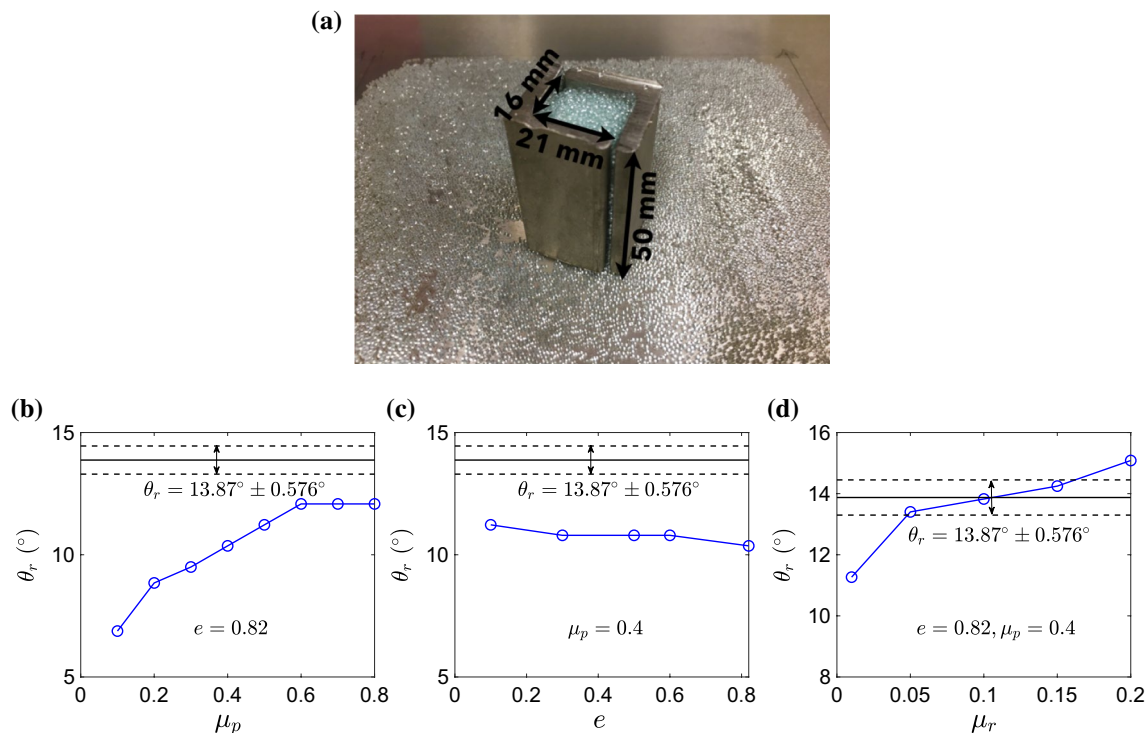
Fig. 6 **a** Setup of the column collapse test, **b** variation of θ_r according to the change of μ_p with a fixed $e = 0.82$, **c** variation of θ_r according to the change of e with a fixed $\mu_p = 0.4$, and **c** variation of θ_r according to the change of μ_r with fixed $\mu_p = 0.4$, $e = 0.82$

0.01 to 0.2. Figure 6d shows the variation of θ_r against μ_r. The numerical results indicate μ_r to be around 0.07 which is slightly larger than 0.01 in [60] where smooth glass spheres were used and slightly smaller than 0.1 in [61] where plastic spheres were used.

Second stage calibration and validation via rotating drum experiments

In the rotating drum experiments (Fig. 7a), after the surface flow becomes stationary under rotation speed $\omega = 2.59°/s, 5.73°/s$ and $11.23°/s$, we use a high speed camera positioned against the glass plate to take images (288 px × 288 px corresponding to a 0.1389 mm/px resolution) for a time period of 10 s with a frame rate of 1000 fps. Accordingly the images cover an area of about 4 cm ×4 cm at the drum center (Fig. 7b). From the sequence of images, we measure the dynamical angle of repose θ_d and the down-stream velocity $v_{yw}(z)$ near the glass plate. In terms of the former, we first binarize each image, then identify the pixels that represents the slope surface, and lastly use the identified pixels to perform a linear fit whose slope gives θ_d (Fig. 7d); as to the latter, we first use the open-source Particle Image Velocimetry (PIV) code [62] to compute the 2D velocity field (v_1, v_2) by correlating

boxes with dimension 8 px ×8 px (corresponding to roughly $\bar{d} \times \bar{d}$), we then compute the velocity field under the frame rotating with the drum located at the drum center to get (v_y, v_z), lastly we compute $v_{yw}(z)$ by averaging v_y within bands ($L_y = 20\bar{d}, L_z = 2\bar{d}$) positioned in parallel to y (slope surface) over a set of points that are placed every $\bar{d}$ distance along z (perpendicular to the slope surface) with $y = 0$. Note that $|v_z| \ll |v_y|$ as the flow is nearly unidirectional. In the simulations, we generate images located at exactly the same location with exactly the same size (and resolution) as the ones taken from experiment (Fig. 7c), from which we follow the same image analysis procedure to find θ_d. For v_{yw}, under the frame rotating with the drum at the drum center, we first pick particles located within $2\bar{d}$ away from the front-side flat wall, we then compute $v_{yw}(z)$ by averaging the particle velocity following the same procedure used in the experiments. Note that the width $2\bar{d}$ is picked to best represent the glass beads that are captured by the high speed camera.

We use θ_d and $v_{yw}(z)$ measured with $\omega = 11.23°/s$ for model calibration and the rest two for model validation. Prior to calibration, according to the column collapse test results, we fix $\mu_p = 0.4$, and $e = 0.82$ that best represents the property of glass beads, although the latter has negligible effect for simulating steady granular flow [57].
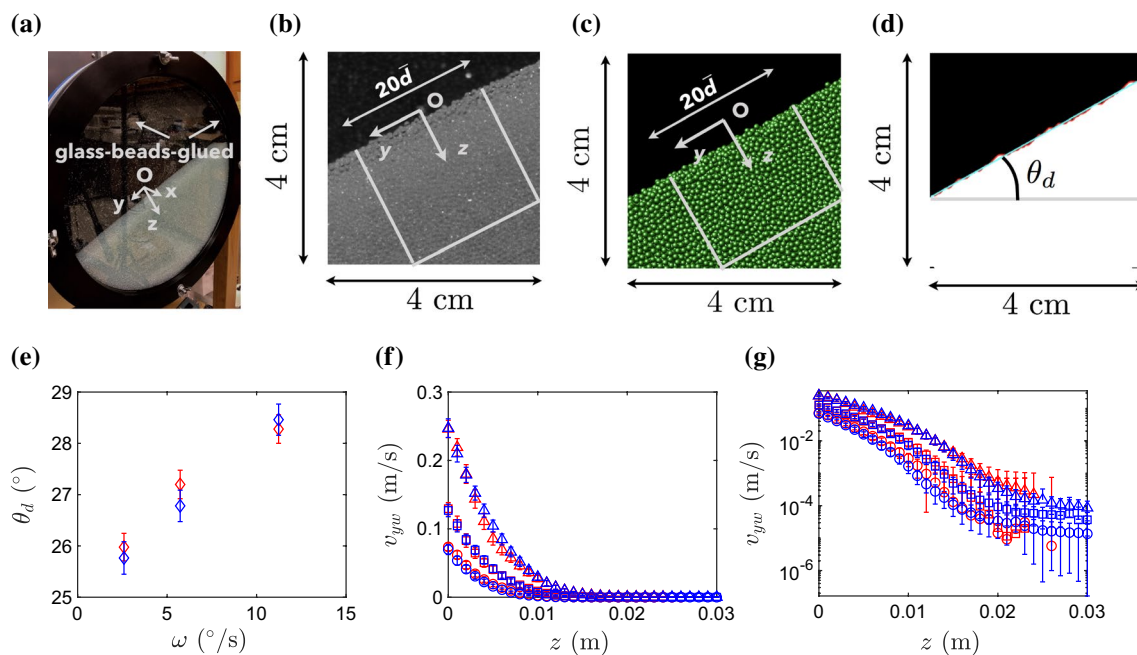

Fig. 7 **a** The half-filled rotating drum with rear-side wall and inner-cylinder wall being glued with glass beads, **b** an image taken by the high speed camera at the drum center, **c** an image generated by numerical simulation with exactly the same location and size (resolution) as (**b**), **d** the binarized image of **c** for θ_d estimation, **e** time-averaged θ_d data for three different rotating speed ω estimated from experiments (red) and simulations (blue), **f** the down-stream velocity profile $v_{yw}(z)$ against the depth at the drum center calculated respectively for $\omega = 11.23°/s$ from experiment (red triangle) and simulation (blue triangle), for $\omega = 5.73°/s$ from experiment (red square) and simulation (blue square), and for $\omega = 2.59°/s$ from experiment (red circle) and simulation (blue circle), and **g** the corresponding semi-log plot of (**f**). For **e–g**, the error bars represent the standard deviation associated with each time-averaged quantity
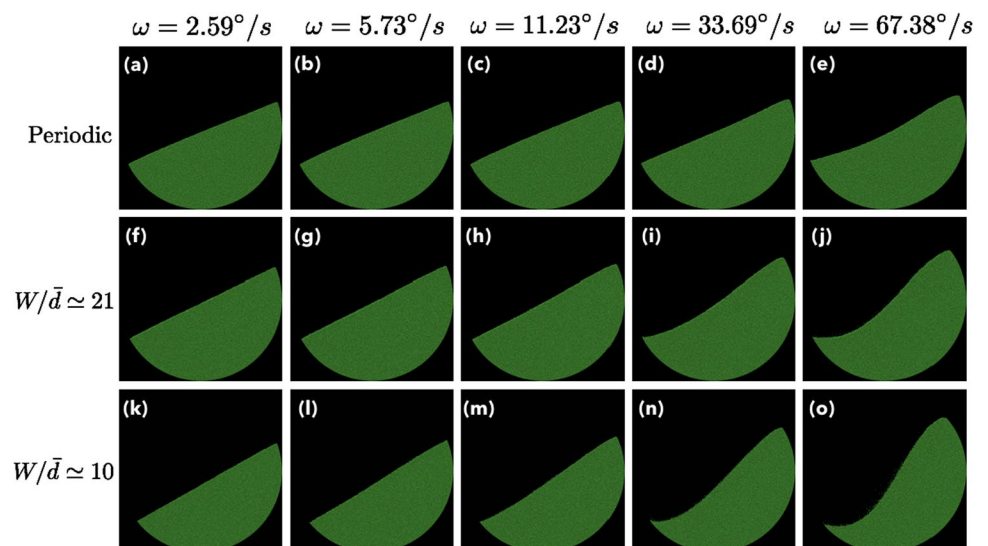
Further, as the front-side plate is also made from glass, we fix the associated wall friction to be 0.4. The only left parameter to calibrate is the inter-particle rolling friction μ_r. Observing Fig. 6d, we vary μ_r to be 0, 0.03, 0.05 and 0.07 and take the particle-wall rolling friction to be zero. As the front-side wall is flat, zero wall rolling friction is a reasonable choice. By solely using θ_d we identify that $\mu_r = 0.03$ gives the best estimation ($\mu_r = 0$ underestimates θ_d while the rest two lead to overestimation). What's more, when $\mu_r = 0.03$, simulation and experiment show excellent agreement (Fig. 7f) in terms of $v_{yw}(z)$. The choice of $\mu_r = 0.03$ is then validated (Fig. 7e–g) by comparing both θ_d and $v_{yw}(z)$ obtained from simulations to those measured from experiments under $\omega = 2.59°/s$ and $\omega = 5.73°/s$.

Appendix 2: Additional simulation results

"S-shape" surface profile

For a direct comparison, Fig. 8 shows the surface shape profile for simulations performed under respectively periodic boundary condition, frictional side walls with $W/\bar{d} \simeq 21$ and wall friction 0.4 and that with $W/\bar{d} \simeq 10$ and wall friction 0.4. It can be observed that as the effective drum width is decreased from infinite (periodic boundaries) to $W/\bar{d} \simeq 21$ and to $W/\bar{d} \simeq 21$, the "S-shape" profile becomes more obvious under more significant side wall friction effect, especially when the rotation speed is large such as when $\omega = 67.38°/s$ (Fig. 8j, o) in our case.

Effect of lateral boundary condition on the co-directionality between s and $\dot{\gamma}^d$

Figure 9 showcases the spatial variation of the misalignment angle α for all considered drum configurations under $\omega = 33.69°/s$, where α is defined as the angle between the principle directions of s and those of $\dot{\gamma}^d$. It can be observed that the presence of frictional side wall has a great impact on the value of α, and the more frictional the side walls and the narrower the drum, the less co-directional are s and $\dot{\gamma}^d$. α is generally large (up to 60°) near the side walls (especially on the bumpy side), and beneath $z = z_{th}$ in the creep flow region. The green solid line indicates locations with local deformation $|\dot{\gamma}^d|/2\Omega$ equalling one [21] where $\Omega = \omega/360°$; locations above this line has $|\dot{\gamma}^d|/2\Omega > 1$ while $|\dot{\gamma}^d|/2\Omega < 1$ for locations below this line. It thus may be understood that the large α in the creep flow region is due to the lack of shear. For locations above $z = z_{th}$, shear deformation is sufficient, and the misalignment α can be attributed to side wall perturbation.

Tests of several non-local models

- *The velocity fluctuation model* Based on 2D numerical simulation results on granular flow in annular shear cells, the model proposed in [44] show that an improved relation between μ and I by adding the effect of velocity fluctuation is able to capture the failure of the one-to-one $\mu(I)$ relation in the creep flow region. The key prerequisite of this model is that the variation of $\mu - I$ and that of $\Delta - I$ are both not one-to-one and are mutually correlated, where $\Delta = |\delta v|\sqrt{\rho_s/P}$ is called the fluctuation number. However, Fig. 10a shows that for all flows considered, there is a global collapse between Δ and I.

Fig. 8 Surface shape profiles. Images in first row from **a**–**e** are those under periodic lateral boundaries, in second row from **f**–**j** represents those under frictional side walls with $W/\bar{d} \simeq 21$, and in third row from **k**–**o** represents those under frictional side walls too but with $W/\bar{d} \simeq 10$. Wall friction is 0.4

Fig. 9 Spatial variation of α under $\omega = 33.69°$/s for all drum configuration considered; from left to right: $W/\bar{d} \simeq 10$ with wall friction of 0.4, periodic boundary, $W/\bar{d} \simeq 21$ with wall friction of 0.2, 0.4, 0.6 and 0.8, respectively. The grey solid lines indicate $z = z_{th}$ and the green ones represent locations with local deformation $|\dot{\gamma}^d|/2\Omega = 1$, where $\Omega = 360°/\omega$
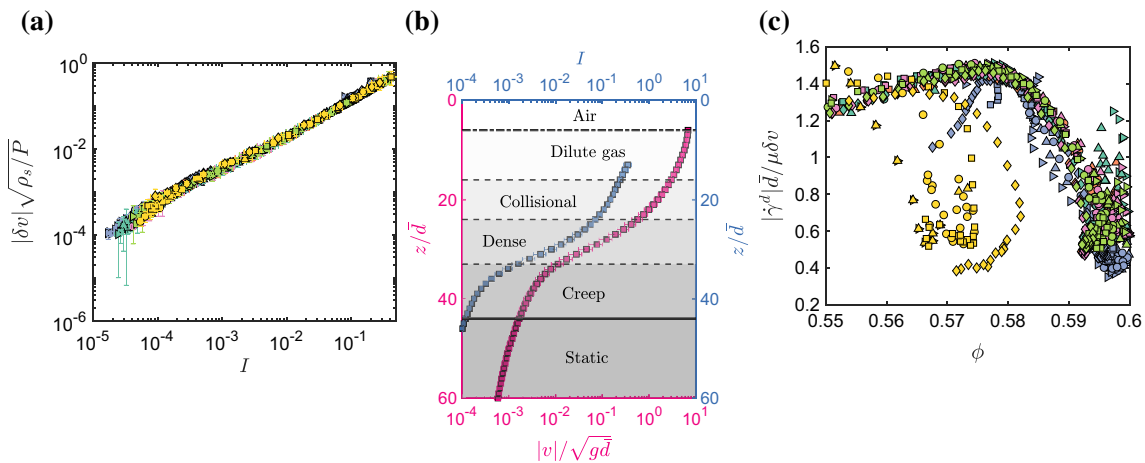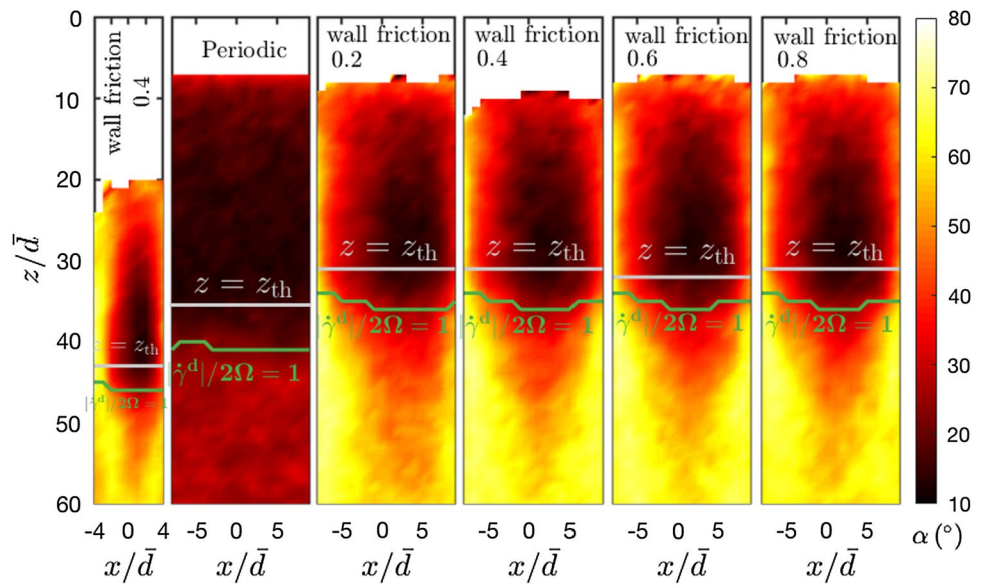

Fig. 10 a $\Delta - I$ data for all cases considered collapse onto a single master curve. Data are shown as the drum-with-average values with error bars representing the associated variation. **b** Variation of drum-width-averaged $|v|/\sqrt{g\bar{d}}$ and I against z with the case under $\omega = 33.69°$/s, $W/d \simeq 21$ and wall friction of 0.4. **c** Relation between the normalized fluidity $|\dot{\gamma}^d|\bar{d}/\mu\delta v$ and volume fraction ϕ. Data are shown as the drum-with-average values for clarity

It appears that this model does not apply to the 3D flows considered in our study.

- *The gradient expansion model* In the gradient expansion model [17], the value of μ in the $\mu - I$ relation is modified by considering an additional contribution $\bar{d}^2\nabla^2 I/I$ which is scaled by a phenomenological constant $\nu > 0$, assuming short range correlation between particle motions in different locations. Physically, the laplacian term captures on average, how does the I value at a certain point compares to its surrounding area. For instance, if a point is surrounded by a more fluid-like area (higher I), the laplacian term is positive and leads to the decrease of μ at that point. Since $\nu > 0$, essentially as long as $\nabla^2 I \neq 0$, the model will report a modification on μ. Figure 10b shows

the typical drum-width-averaged I and $|v|/\sqrt{g\bar{d}}$ against z with the case under $\omega = 33.69°$/s, $W/d \simeq 21$ and wall friction of 0.4. The variation of I against z roughly follows the same trend as that of $|v|/\sqrt{g\bar{d}}$: it linearly decays in the collisional region and exponentially decays in the dense region. Thus in the collisional region $\nabla^2 I = 0$ and the model reports no modification on μ, which is consistent with our observation. However, in the dense region, μ will be modified according to the model since $\nabla^2 I \neq 0$ —this contradicts our computations that confirm the applicability of the $\mu - I$ relation in the dense region. Again, it appears that this model does not apply to the 3D surface flows considered in our study.

Fig. 11 Spatial variation of the coordination number Z and a_χ^v against the depth z. The symbol shape represents different rotation speed, while the symbol color represents different drum configurations in terms of drum width W and side wall friction. Error bars represent the variation of each shown quantity across the drum width
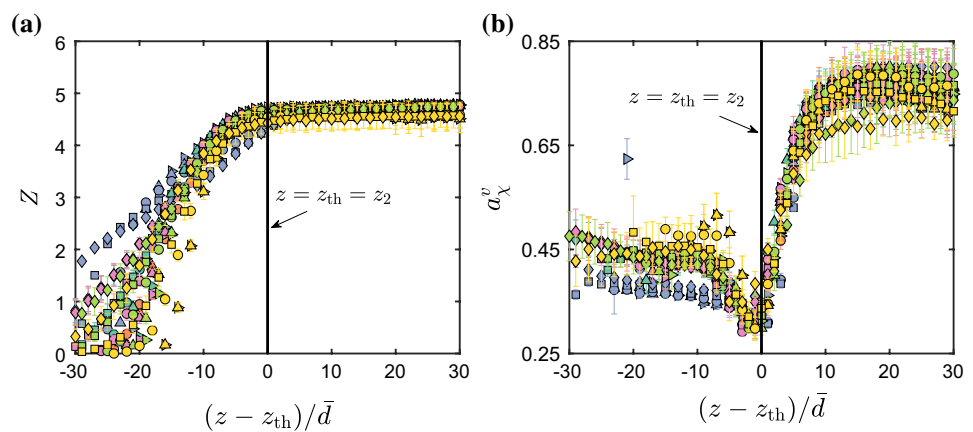
- *The fluidity model* The fluidity model [16] implicitly modifies the value of μ in the $\mu - I$ relation by considering the nearby region contribution through the Laplacian of the fluidity parameter $g = \dot{\gamma}/\mu$ expressed as $\xi^2 \nabla^2 g$, where ξ is defined as the cooperative length that diverges as approaching the jamming transition. Although the mathematical expression looks similar to that of the gradient expansion model, the assumed underlying physical mechanism is different. g is found to obey the following microscopic relation [29]: $\dot{\gamma}^d \bar{d}/\mu = \delta v F(\phi)$. Figure 10c shows how the normalized fluidity $\dot{\gamma}^d \bar{d}/(\mu \delta v)$, varies with volume fraction ϕ. It can be observed for all data computed from $W/\bar{d} \simeq 21$ with varying side wall friction, they collapse well onto a single curve who shape resembles the one identified in [29]. However, this curve is clearly drum-width-dependent, as when the effective drum width is respectively infinite (periodic boundary, colored in blue) and $10\bar{d}$ (colored in yellow), no collapse can be observed, even in the dense and collisional region where the $\mu(I)$ rheology in its invariant form holds. Memory effect (insufficient shear) observed for $I < I_{th}$ (see Fig. 9) may explain the failure of the model in the creep flow region; while its break down in the fast flow regime ($I > I_{th}$ with sufficient shear deformation) reveals the non-trivial effects of side wall friction that have not been considered in the granular fluidity model [29]—indeed, even though investigated in 3D configuration, the considered flow fields have shear only in z direction as boundaries along both x and y direction are treated as periodic.

Additional results from micro-scale analysis

The micro-structure can be investigated by three kinds of quantities that range from lower-order (L) to higher-order (H) within each kind: (1) geometry-associated ones range from volume fraction ϕ (L), coordination number Z (L) to the angular distribution of contact orientation (H) [47, 48];

(2) inter-particle-force-associated ones range from normal (and tangential) force p.d.f. distribution (L) [47, 48] to their angular distributions (H) [47, 48]; and (3) kinematics-associated ones where the lower order quantity can be the velocity fluctuation δv [29, 44]. Inspired by [48, 63], we may regard $a_\chi^v = (\lambda_3 - \lambda_1)/(\lambda_3 + \lambda_1)$ as the higher order quantity where $\lambda_3(\lambda_1)$ is the maximum (minimum) eigenvalue of the tensor $\chi = \langle |\delta v| n_i^v n_j^v \rangle / \langle |\delta v| \rangle$. Here "$\langle \cdot \rangle$" denotes the average over all particles and n^v is the direction of velocity fluctuation associated with each particle. Accordingly a_χ^v has range from 0 to 1 and reflects how "cooperative" the particle motions are: a value close to 1 in the quasi-static flow region implies the formation of "granular eddy" [24, 64].

In principle, we are trying to find certain micro-structural quantities whose variations against I, (R1) exhibit a clear transition as passing through $z = z_{th}$, and more importantly, (R2) show consistence with that of μ against I for rheological considerations: when $I > z_{th}$ they are free of drum configuration effect and rotation speed effect while they become lateral boundary dependent and rotation speed dependent as soon as $I \leq I_{th}$. Many of the aforementioned quantities, as we discover, only satisfy R1, such as Z and a_χ^v. Figure 11a shows the variation of Z against the depth z. Z varies case by cases when $z \leq z_{th}$ and remains almost constant when $z > z_0$. However, on the contrary, the stress ratio μ shows a global collapse when $z \leq z_{th}$ but varies case by case when $z > z_{th}$. a_χ^v shows a slightly different spatial variation (Fig. 11b): it remains constant when $z \leq z_{th}$ in a similar way to that of $\delta\theta$. However, a_χ^v seems to be boundary condition dependent instead. When $z > z_{th}$, it rapidly increases independently with respect to the boundary condition and rotation speed, which is inconsistent with the variation of μ either. Following the momentum transferring argument, we have also investigated the portion of formed granular clusters based on either the velocity fluctuation following [5, 64] or the

Fig. 12 $|v|(z)$ profile variation across the drum width for different rotation speeds with each color representing a certain location x between $-8\bar{d}$ and $9\bar{d}$ ($W/\bar{d} \simeq 21$) and between $-3\bar{d}$ and $4\bar{d}$ ($W/\bar{d} \simeq 10$). First row from **a**–**e**: data extracted from simulations with periodic lateral boundaries; second row from **f**–**j**: data extracted from simulations with frictional side walls ($W/\bar{d} \simeq 21$); third row from **k**–**o**: data extracted from simulations with frictional side walls ($W/\bar{d} \simeq 10$); wall friction is 0.4
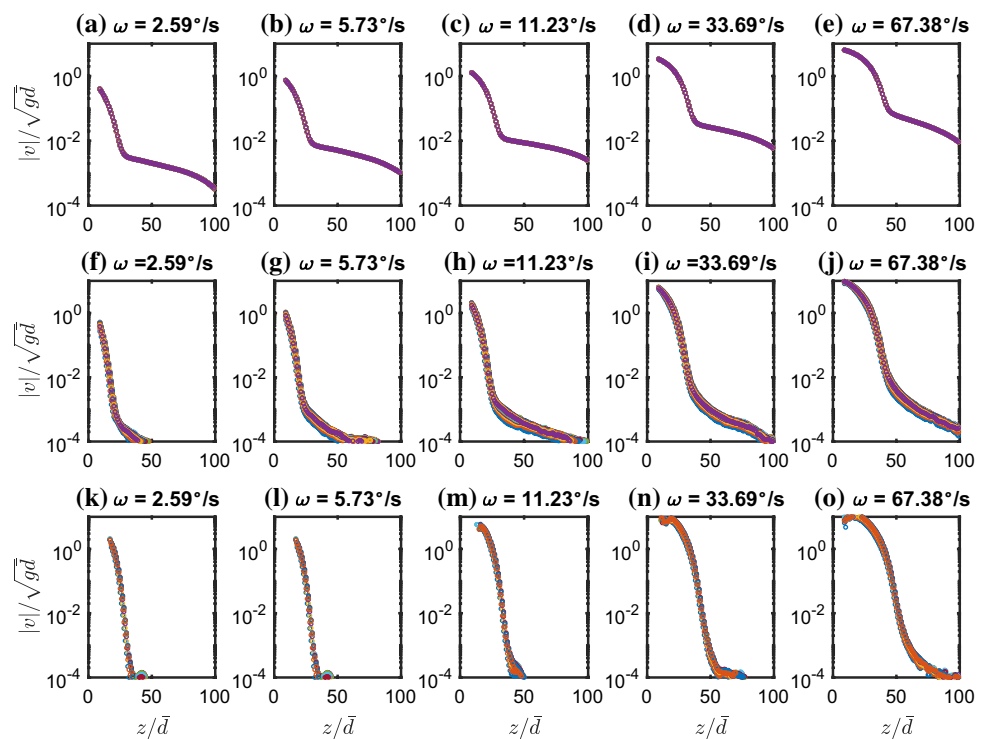
local volume fraction fluctuation (achievable via the computed Voronoi diagram) following [5, 14]. The variation of such portion along the depth show similar trend as that of a_{χ}^{v} that does not satisfy (R2).

Determination of z_{th} based on the drum-width-averaged velocity profile

Figure 12 shows the velocity magnitude profile against depth at the drum center $|v|(z)$ and its variation across the drum width, for the same set of simulations considered here. When the lateral boundaries are periodic, $|v|(z)$ shows negligible differences across the drum width. For the cases with frictional side walls ($W/\bar{d} \simeq 21$ and 10), $|v|(z)$ varies majorly as vertical translation without shape alteration. Therefore without sacrificing much the accuracy we determine z_{th} based on the drum-width-averaged $|v|(z)$ profile.

References

1. Jaeger, H.M., Nagel, S.R., Behringer, R.P.: Granular solids, liquids, and gases. Rev. Mod. Phys. **68**(4), 1259 (1996)
2. Mueth, D.M., Debregeas, G.F., Karczmar, G.S., Eng, P.J., Nagel, S.R., Jaeger, H.M.: Signatures of granular microstructure in dense shear flows. Nature **406**(6794), 385 (2000)
3. Komatsu, T.S., Inagaki, S., Nakagawa, N., Nasuno, S.: Creep motion in a granular pile exhibiting steady surface flow. Phys. Rev. Lett. **86**(9), 1757 (2001)
4. Bonamy, D., Daviaud, F., Laurent, L.: Experimental study of granular surface flows via a fast camera: a continuous description. Phys. Fluids **14**(5), 1666–1673 (2002)
5. Bonamy, D., Daviaud, F., Laurent, L., Bonetti, M., Bouchaud, J.P.: Multiscale clustering in granular surface flows. Phys. Rev. Lett. **89**(3), 034301 (2002)
6. Choi, J., Kudrolli, A., Rosales, R.R., Bazant, M.Z.: Diffusion and mixing in gravity-driven dense granular flows. Phys. Rev. Lett. **92**(17), 174301 (2004)
7. Forterre, Y., Pouliquen, O.: Flows of dense granular media. Annu. Rev. Fluid Mech. **40**, 1–24 (2008)
8. MiDi, G.: On dense granular flows. Eur. Phys. J. E **14**(4), 341–365 (2004)
9. da Cruz, F., Emam, S., Prochnow, M., Roux, J.-N., Chevoir, F.: Rheophysics of dense granular materials: discrete simulation of plane shear flows. Phys. Rev. E **72**(2), 021309 (2005)
10. Jop, P., Forterre, Y., Pouliquen, O.: A constitutive law for dense granular flows. Nature **441**, 727–730 (2006)
11. Baran, O., Ertaş, D., Halsey, T.C., Grest, G.S., Lechman, J.B.: Velocity correlations in dense gravity-driven granular chute flow. Phys. Rev. E **74**(5), 051302 (2006)
12. Staron, L.: Correlated motion in the bulk of dense granular flows. Phys. Rev. E **77**(5), 051304 (2008)
13. Orpe, A.V., Kudrolli, A.: Velocity correlations in dense granular flows observed with internal imaging. Phys. Rev. Lett. **98**(23), 238001 (2007)
14. Mills, P., Rognon, P., Chevoir, F.: Rheology and structure of granular materials near the jamming transition. EPL (Europhys. Lett.) **81**(6), 64005 (2008)
15. Pouliquen, O., Forterre, Y.: A non-local rheology for dense granular flows. Philos. Trans. R. Soc. Lond. A Math. Phys. Eng. Sci. **367**(1909), 5091–5107 (2009)
16. Kamrin, K., Koval, G.: Nonlocal constitutive relation for steady granular flow. Phys. Rev. Lett. **108**(17), 178301 (2012)

17. Bouzid, M., Trulsson, M., Claudin, P., Clément, E., Andreotti, B.: Nonlocal rheology of granular flows across yield conditions. Phys. Rev. Lett. **111**(23), 238301 (2013)

18. Bouzid, M., Izzet, A., Trulsson, M., Clément, E., Claudin, P., Andreotti, B.: Non-local rheology in dense granular flows. Eur. Phys. J. E **38**(11), 125 (2015)

19. de Coulomb, A.F., Bouzid, M., Claudin, P., Clément, E., Andreotti, B.: Rheology of granular flows across the transition from soft to rigid particles. Phys. Rev. Fluids **2**(10), 102301 (2017)

20. Saitoh, K., Tighe, B.P.: Nonlocal effects in inhomogeneous flows of soft athermal disks. Phys. Rev. Lett. **122**(18), 188001 (2019)

21. Cortet, P.-P., Bonamy, D., Daviaud, F., Dauchot, O., Dubrulle, B., Renouf, M.: Relevance of visco-plastic theory in a multi-directional inhomogeneous granular flow. EPL (Europhys. Lett.) **88**(1), 14001 (2009)

22. Renouf, M., Bonamy, D., Dubois, F., Alart, P.: Numerical simulation of two-dimensional steady granular flows in rotating drum: on surface flow rheology. Phys. Fluids **17**(10), 103303 (2005)

23. Fan, Y., Umbanhowar, P.B., Ottino, J.M., Lueptow, R.M.: Shear-rate-independent diffusion in granular flows. Phys. Rev. Lett. **115**(8), 088001 (2015)

24. Miller, T., Rognon, P., Metzger, B., Einav, I.: Eddy viscosity in dense granular flows. Phys. Rev. Lett. **111**(5), 058002 (2013)

25. Azéma, E., Radjai, F.: Internal structure of inertial granular flows. Phys. Rev. Lett. **112**(7), 078001 (2014)

26. Jop, P., Forterre, Y., Pouliquen, O.: Crucial role of sidewalls in granular surface flows: consequences for the rheology. J. Fluid Mech. **541**, 167–192 (2005)

27. Pohlman, N.A., Ottino, J.M., Lueptow, R.M.: End-wall effects in granular tumblers: from quasi-two-dimensional flow to three-dimensional flow. Phys. Rev. E **74**(3), 031305 (2006)

28. Du Pont, S.C., Gondret, P., Perrin, B., Rabaud, M.: Wall effects on granular heap stability. EPL (Europhys. Lett.) **61**(4), 492 (2003)

29. Zhang, Q., Kamrin, K.: Microscopic description of the granular fluidity field in nonlocal flow modeling. Phys. Rev. Lett. **118**(5), 058001 (2017)

30. Cundall, P .A., Strack, O .D.: A discrete numerical model for granular assemblies. Geotechnique **29**(1), 47–65 (1979)

31. Kloss, C., Goniva, C., Hager, A., Amberger, S., Pirker, S.: Models, algorithms and validation for opensource DEM and CFD–DEM. Prog. Comput. Fluid Dyn. Int. J. **12**(2–3), 140–152 (2012)

32. Börzsönyi, T., Ecke, R.E., McElwaine, J.N.: Patterns in flowing sand: understanding the physics of granular flow. Phys. Rev. Lett. **103**(17), 178302 (2009)

33. Cheng, H., Shuku, T., Thoeni, K., Yamamoto, H.: Probabilistic calibration of discrete element simulations using the sequential quasi-monte carlo filter. Granul. Matter **20**(1), 11 (2018)

34. Turkia, S.B., Wilke, D.N., Pizette, P., Govender, N., Abriak, N.-E.: Benefits of virtual calibration for discrete element parameter estimation from bulk experiments. Granul. Matter **21**(4), 110 (2019)

35. Richard, P., Valance, A., Métayer, J.-F., Sanchez, P., Crassous, J., Louge, M., Delannay, R.: Rheology of confined granular flows: scale invariance, glass transition, and friction weakening. Phys. Rev. Lett. **101**(24), 248002 (2008)

36. Artoni, R., Richard, P.: Effective wall friction in wall-bounded 3d dense granular flows. Phys. Rev. Lett. **115**(15), 158001 (2015)

37. Brodu, N., Richard, P., Delannay, R.: Shallow granular flows down flat frictional channels: steady flows and longitudinal vortices. Phys. Rev. E **87**(2), 022202 (2013)

38. Taberlet, N., Richard, P., Valance, A., Losert, W., Pasini, J.M., Jenkins, J.T., Delannay, R.: Superstable granular heap in a thin channel. Phys. Rev. Lett. **91**(26), 264301 (2003)

39. Taberlet, N., Richard, P., Hinch, E.J.: S shape of a granular pile in a rotating drum. Phys. Rev. E **73**(5), 050301(R) (2006)

40. Christoffersen, J., Mehrabadi, M., Nemat-Nasser, S.: A micro-mechanical description of granular material behavior. J. Appl. Mech. **48**(2), 339–344 (1981)

41. Rycroft, C.H., Grest, G.S., Landry, J.W., Bazant, M.Z.: Analysis of granular flow in a pebble-bed nuclear reactor. Phys. Rev. E **74**(2), 021306 (2006)

42. Camenen, J.-F., Descantes, Y., Richard, P.: Effect of confinement on dense packings of rigid frictionless spheres and polyhedra. Phys. Rev. E **86**(6), 061317 (2012)

43. Koval, G., Roux, J.-N., Corfdir, A., Chevoir, F.: Annular shear of cohesionless granular materials: from the inertial to quasi-static regime. Phys. Rev. E **79**(2), 021306 (2009)

44. Gaume, J., Chambon, G., Naaim, M.: Quasistatic to inertial transition in granular materials and the role of fluctuations. Phys. Rev. E **84**(5), 051304 (2011)

45. Azéma, E., Descantes, Y., Roquet, N., Roux, J.-N., Chevoir, F.: Discrete simulation of dense flows of polyhedral grains down a rough inclined plane. Phys. Rev. E **86**(3), 031303 (2012)

46. Goldhirsch, I.: Rapid granular flows. Annu. Rev. Fluid Mech. **35**(1), 267–293 (2003)

47. Azéma, E., Radjai, F., Dubois, F.: Packings of irregular polyhedral particles: strength, structure, and effects of angularity. Phys. Rev. E **87**(6), 062203 (2013)

48. Rothenburg, L., Bathurst, R.: Analytical study of induced anisotropy in idealized granular materials. Geotechnique **39**(4), 601–614 (1989)

49. Börzsönyi, T., Szabó, B., Törös, G., Wegner, S., Török, J., Somfai, E., Bien, T., Stannarius, R.: Orientational order and alignment of elongated particles induced by shear. Phys. Rev. Lett. **108**(22), 228302 (2012)

50. Hidalgo, R., Szabó, B., Gillemot, K., Börzsönyi, T., Weinhart, T.: Rheological response of nonspherical granular flows down an incline. Phys. Rev. Fluids **3**(7), 074301 (2018)

51. Nadler, B., Guillard, F., Einav, I.: Kinematic model of transient shape-induced anisotropy in dense granular flow. Phys. Rev. Lett. **120**(19), 198003 (2018)

52. Gray, J.M.N.T.: Particle segregation in dense granular flows. Annu. Rev. Fluid Mech. **50**, 407–433 (2018)

53. Cantor, D., Azéma, E., Sornay, P., Radjai, F.: Rheology and structure of polydisperse three-dimensional packings of spheres. Phys. Rev. E **98**(5), 052910 (2018)

54. Mandal, S., Khakhar, D.: Sidewall-friction-driven ordering transition in granular channel flows: implications for granular rheology. Phys. Rev. E **96**(5), 050901(R) (2017)

55. Jean, M.: The non-smooth contact dynamics method. Comput. Methods Appl. Mech. Eng. **177**(3–4), 235–257 (1999)

56. Pazouki, A., Kwarta, M., Williams, K., Likos, W., Serban, R., Jayakumar, P., Negrut, D.: Compliant contact versus rigid contact: a comparison in the context of granular dynamics. Phys. Rev. E **96**(4), 042905 (2017)

57. Silbert, L.E., Ertaş, D., Grest, G.S., Halsey, T.C., Levine, D., Plimpton, S.J.: Granular flow down an inclined plane: Bagnold scaling and rheology. Phys. Rev. E **64**(5), 051302 (2001)

58. Reagle, C., Delimont, J., Ng, W., Ekkad, S., Rajendran, V.: Measuring the coefficient of restitution of high speed microparticle impacts using a PTV and CFD hybrid technique. Meas. Sci. Technol. **24**(10), 105303 (2013)

59. Zhou, Y., Wright, B., Yang, R., Xu, B.H., Yu, A.-B.: Rolling friction in the dynamic simulation of sandpile formation. Physica A **269**(2–4), 536–553 (1999)

60. Frankowski, P. Morgeneyer, M.: Calibration and validation of DEM rolling and sliding friction coefficients in angle of repose and shear measurements, In: AIP Conference Proceedings, vol. 1542, pp. 851–854. AIP (2013)

61. Phillip Grima, A., Wilhelm Wypych, P.: Discrete element simulations of granular pile formation: method for calibrating discrete element models. Eng. Comput. **28**(3), 314–339 (2011)

62. Thielicke, W., Stamhuis, E.: PIVlab-towards user-friendly, affordable and accurate digital particle image velocimetry in matlab. J. Open Res. Softw. **2**(1), e30

63. Radjai, F., Roux, S.: Turbulentlike fluctuations in quasistatic flow of granular media. Phys. Rev. Lett. **89**(6), 064302 (2002)

64. Kharel, P., Rognon, P.: Vortices enhance diffusion in dense granular flows. Phys. Rev. Lett. **119**(17), 178001 (2017)